npj | Computational Materials

www.nature.com/npjcompumats

REVIEW ARTICLE OPEN

Chemomechanical modeling of lithiation-induced failure in high-volume-change electrode materials for lithium ion batteries

Sulin Zhang[1]

The rapidly increasing demand for efficient energy storage systems in the last two decades has stimulated enormous efforts to the development of high-capacity, high-power, durable lithium ion batteries. Inherent to the high-capacity electrode materials is material degradation and failure due to the large volumetric changes during the electrochemical cycling, causing fast capacity decay and low cycle life. This review surveys recent progress in continuum-level computational modeling of the degradation mechanisms of high-capacity anode materials for lithium-ion batteries. Using silicon (Si) as an example, we highlight the strong coupling between electrochemical kinetics and mechanical stress in the degradation process. We show that the coupling phenomena can be tailored through a set of materials design strategies, including surface coating and porosity, presenting effective methods to mitigate the degradation. Validated by the experimental data, the modeling results lay down a foundation for engineering, diagnosis, and optimization of high-performance lithium ion batteries.

npj Computational Materials (2017)3:7 ; doi:10.1038/s41524-017-0009-z

INTRODUCTION

Since its discovery, lithium (Li)-ion battery (LIB) has become the primary power source for various portable electronics in today's mobile society and been extended to electric vehicles. Despite the impressive market share, the current LIB technologies cannot meet the rapidly growing demand for high energy density and long cycle life of batteries. This has motivated enormous efforts for developing new-generation LIBs that are of not only high energy and high power, but also long cycle life.[1–6] Unfortunately, high-capacity electrode materials, such as Si, are susceptible to chemomechanical degradation and failure owing to the large volume change during electrochemical cycling, leading to fast capacity loss and short cycle life. Understanding of the chemomechanical degradation mechanisms is thus imperative for the design of durable next-generation LIBs.

Several possible processes contribute to the degradation of the high-volume-change electrode materials (see Fig. 1). First, lithiation-induced large volumetric expansion tends to generate stress concentration, leading to the chemomechanical fracture of the electrodes.[7–12] The fracture consequently causes the loss of electrical contact between active materials, current collectors, and electrolytes, resulting in rapid capacity fading and poor cyclability (Fig. 1a). Second, lithiation induces large compressive stress inside the active materials, which slows down further lithiation, i.e., lithiation retardation (Fig. 1b). In severe cases, the large compressive stress completely arrests lithiation, and the inner core of the active materials becomes inaccessible to the electrolyte, leading to a reduced effective capacity. Third, the large volumetric changes during the lithiation/delithiation cycles cause repeated breaking and forming of the solid electrolyte interface (SEI) film on the active materials, resulting in unstable SEI growth[13] and converting cycleable live lithiums in the electrode and electrolyte to dead lithiums in SEI (Fig. 1c), eventually leading to lithium exhaustion and battery death.

Over the last several years, various experimental techniques, including nanoindentation,[14–16] wafer curvature method,[17–23] etc., have been employed to characterize the degradation of the electrode materials at different stages of charge. In particular, a nanobattery platform[24] for in situ TEM testing, and characterization has been developed for real-time imaging of the chemical reaction, ion transport, phase transformation, defect nucleation and growth during electrochemical cycling. These experimental data provide insights for establishing physically based models. In parallel to these experiments, models of different length scales have been established, ranging from first-principles simulations,[25–36] molecular dynamics with empirical force fields on the atomic scale,[37–42] continuum-level simulations that couple field equations dictating Li transport and mechanical equilibrium.[9, 12, 43–55] Together, this has opened a bottom-up avenue for developing high-performance LIBs, in contrast to the top-down approach adopted by the conventional battery development.

This review summarizes the recent progress in the continuum-level modeling of chemomechanical degradation of high-capacity electrode materials. We first lay down the coupled field equations for lithium transport and mechanical equilibrium. Examples are then given on how the electrochemistry–mechanics coupling defines the degradation, followed by a discussion of the design strategies that mitigate the degradation. Finally, we conclude and give perspectives of the field.

LITHIATION MECHANISMS

A battery is an energy storage device that converts chemical energy into electrical energy.[56] A battery consists of a collection of electrochemical cells, each composed of two electrodes separated

[1]Department of Engineering Science and Mechanics, and Materials Research Institute, The Pennsylvania State University, University Park, PA 16802, USA
Correspondence: Sulin Zhang (suz10@psu.edu)

Received: 21 July 2016 Revised: 2 November 2016 Accepted: 16 January 2017
Published online: 17 February 2017

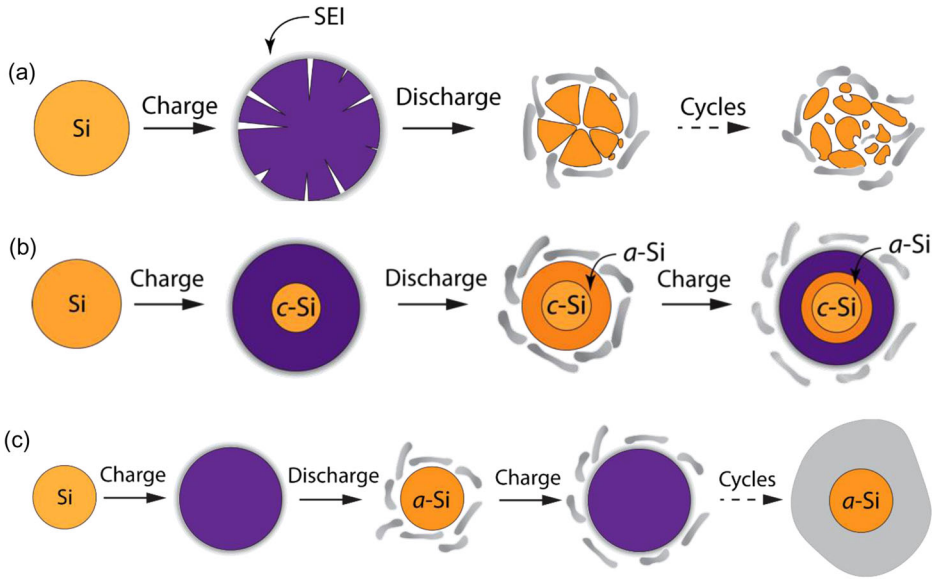

Fig. 1 Degradation mechanisms of large-volume-change anodes in LIBs. **a** Fracture and pulverization of high-capacity electrode materials. **b** Lithiation retardation due to compressive stress reduces rate performance and lowers the effective capacity. **c** Large volume changes induce unstable SEI growth on the electrode surface

by an electrolyte. LIBs function by shuttling Li ions between the electrodes through the electrolyte. Under the operation condition (discharging), Li ions migrate from the negative (anode) to the positive (cathode) electrodes through the electrolyte, driven by the electrochemical potential difference of the ions. Meanwhile, electrons flow from the anode to the cathode through the external wires, generating electrical current to power the external working load. During charging, the reverse process occurs.

Lithiation/delithiation of materials with a layered structure generally features an intercalation mechanism, wherein Li ions are reversibly inserted into and extracted from the interlayers[57, 58] (Fig. 2a1, a2). The intercalation mechanism induces relatively small-volume expansion, which ensures structural stability, capacity retention, and long cycle life. For these reasons, graphite, the layered graphene, exhibits stable working voltage and good cycle performance. Along with its high conductivity, graphite is the primary anode material in the currently commercial LIBs.[59] A downside of this insertion mechanism is the relatively low specific capacity limited by the available Li insertion sites. The theoretical capacity of graphite is only ~372 mAh/g (forming LiC_6 compound),[60, 61] inadequate for high-energy-density applications.

Alloying is another lithiation mechanism for a variety of high-capacity anode materials, including Si, Sn, Ge, Al, Ga, etc. Alloying with Li involves bond breaking/forming and solid-state amorphization, and the capacity is not limited by the available insertion sites (Fig. 2b1–3). As the leading anode candidate for LIBs, Si has a theoretical specific capacity of 4200 mAh/g[59, 61–63] when alloyed to $Li_{22}Si_5$, one order of magnitude higher than that of graphite. However, the large insertion/deinsertion of Li into Si induces huge volumetric changes (~300%), causing electro-chemomechanical failure of the batteries, discussed previously.

COUPLING BETWEEN LITHIATION KINETICS AND MECHANICAL STRESS

Governing equations

From a continuum point of view, Li transport and stress generation are described by field variables, i.e., Li concentration $c(\mathbf{x};t)$and the Cauchy stress $\sigma(\mathbf{x};t)$; both spatiotemporally vary. The dynamic evolutions of these two field variables are coupled, as described below.

Stress-mediated Li diffusion. Li transport in the host materials can be described by the diffusion equation, as

$$\frac{\partial c}{\partial t} + \nabla \cdot \boldsymbol{j} = 0 \qquad \text{in } V \tag{1}$$

where $\boldsymbol{j}$ is the flux, and V is the volume of the electrode. The gradient of the diffusional potential of Li μ serves as the driving force for Li diffusion:

$$\boldsymbol{j} = -\boldsymbol{M} \cdot \nabla \mu, \tag{2}$$

where $\boldsymbol{M}$ is the mobility tensor, which is generally a function of Li concentration c. The diffusional potential is related to the Li concentration and the local stress state σ: $\mu = \mu(c;\sigma)$. In this setting, the hydrostatic stress gradient functions as a part of the driving force for the Li diffusion,[64, 65] in addition to the Li concentration gradient.

An alternative approach is to still adopt the classical Fick's first law, $\boldsymbol{j} = -D\nabla c$, but embedding the stress effect by empirically assuming Li diffusivity as a function of both Li concentration and the stress state,[12, 66, 67] i.e., $D = D(c;\sigma)$. The effective diffusivity can be expressed by $D = D_0\, exp(-p\Omega/k_BT)$, where D_0 is the diffusivity at the stress-free condition, p is the hydrostatic pressure, Ω is the activation volume and k_BT is the thermal energy.

In addition to the constitutive relations for Li transport, the diffusion equation must be solved by supplementing with boundary conditions at the surface of the electrodes. Since surface diffusivity is generally much larger than bulk diffusivity, the Dirichlet boundary condition can be imposed, as

$$c = 1 \qquad \text{on } S. \tag{3}$$

Lithiation-mediated deformation and stress generation. As the time scale associated with the mechanical process is much shorter than diffusion, we assume that mechanical equilibrium is met at any instant during lithiation process:

$$\nabla \cdot \boldsymbol{\sigma} = 0 \qquad \text{in } V. \tag{4}$$

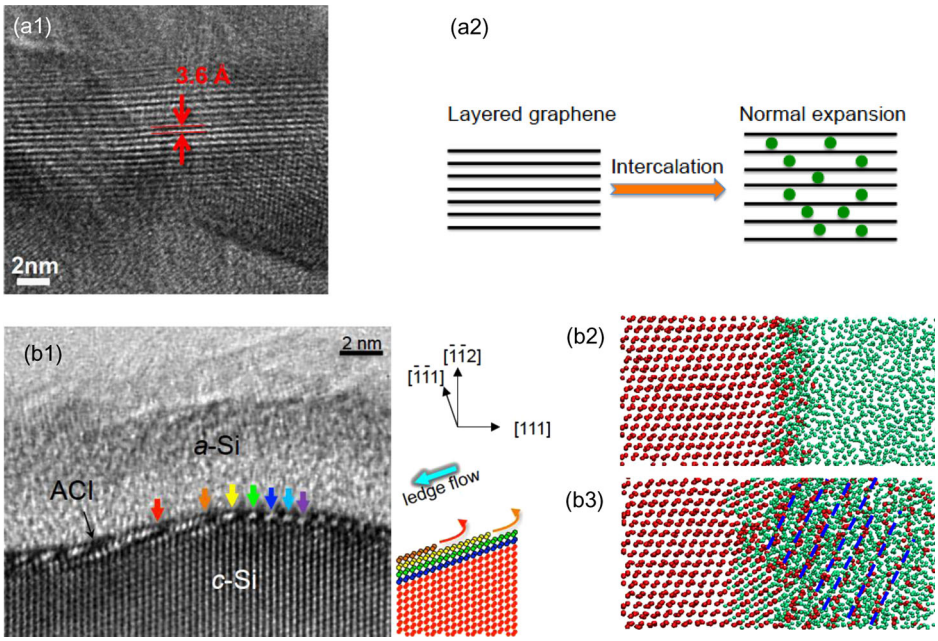

Fig. 2 Two typical lithiation mechanisms: intercalation (e.g., layered graphene) vs. alloying (e.g., Si). **a**1 A TEM image shows Li intercalation to layered graphene, causing interlayer expansion from 3.4 Å to 3.6 Å.[53] **a2** Schematics showing Li intercalation into layered graphene. **b1** A TEM image showing alloying of *c*-Si during lithiation, involving bond breaking, directional ledge flow, layered-by-layer peel-off, and solid-state amorphization.[81] **b2**, **b3** Two sequential snapshots from atomistic simulations showing the amorphization process in *c*-Si during lithiation

For free-standing specimens, a traction-free boundary condition can be imposed, as

$$\boldsymbol{n}\cdot\boldsymbol{\sigma}=0 \qquad \text{on } S, \tag{5}$$

where $\boldsymbol{n}$ is the outward normal of the outer surface S of the electrode exposing to Li.

In the finite strain kinematics, the total stretch rate tensor $\boldsymbol{d}$ can be decomposed into three additive parts,

$$\boldsymbol{d}=\boldsymbol{d}^{\mathrm{c}}+\boldsymbol{d}^{\mathrm{e}}+\boldsymbol{d}^{\mathrm{p}}, \tag{6}$$

where $\boldsymbol{d}^{\mathrm{c}}$, $\boldsymbol{d}^{\mathrm{e}}$, and $\boldsymbol{d}^{\mathrm{p}}$ are the chemical, elastic, and plastic stretch rates, respectively.[68–72] The additional chemical strain rate $\boldsymbol{d}^{\mathrm{c}}$ is proportional to the increment of the Li concentration

$$\boldsymbol{d}^{\mathrm{c}}=\dot{c}\boldsymbol{\beta}, \tag{7}$$

embodying the effect of lithiation on mechanics, where $\boldsymbol{\beta}$ is the lithiation-induced expansion tensor. One notices that the chemical strain is analogous to the thermal strain in formulation by considering $\boldsymbol{\beta}$ as the coefficient of thermal expansion and c the temperature. In general, $\boldsymbol{\beta}$ can be anisotropic and adopts different values in the three dilational directions.

In the finite-strain framework, the constitutive relations for elastic and plastic parts are formulated in rate form, where the elastic and plastic stretch rates, and the elastic spin are related to the stress rate. The unlithiated domain is modeled as an isotropic, elastic material, whose stress and strain rates obey the classical Hooke's law with two material constants, Young's modulus Y and Poisson's ratio ν. The lithiated phase is modeled by an isotropic elastic, perfectly,[65] or rate-dependent plastic material,[67, 70, 73–77] with phase-dependent elastic constants. Note that the rate-dependent plasticity introduces an additional time scale characterizing the stress relaxation, and thus may affect stress generation. The plastic stretch rate, $\boldsymbol{d}^{\mathrm{p}}$, obeys the associated J_2-flow rule. These constitutive relations are necessary for solving the governing equations listed above.

The moving phase boundary. Lithiation of Si or many other high-capacity anode materials features a moving phase boundary (i.e., the reaction front) that separates the lithiated (Li-rich) and unlithiated (Li-poor) phases. The characteristics of the reaction front for different electrode materials or at different electrochemical stages vary. The reaction front is atomically sharp (~1 nm) in *c*-Si;[78] but diffuse in *a*-Si during the second-step lithiation.[79, 80] The width of the phase boundary critically modulates the stress generation and localization. To simplify the analysis, Yang *et al*. simulated the phase boundary motion by diffusion, rather than reaction, despite the clear difference between these two transport processes.[9, 12, 67] With this simplification, Li transport, which involves chemical reaction and solid-state diffusion in series, can be described by diffusion (Eq. 1) in a unified manner. To produce a sharp phase (two-phase) boundary with an abrupt change of Li concentration, Li diffusivity to be a nonlinear function of Li concentration in the entire system:

$$D=D_0\left[\frac{1}{(1-c)}-2ac\right]. \tag{8}$$

where D_0 is a diffusion constant and a is a tunable constant that controls the concentration profile near the phase boundary.[8, 9] The singular function yields considerably large Li diffusivity in the lithiated domain ($c\to1$), but a finite value (D_0) close to the unlithiated domain ($c=1$). This effectively generates a sharp interface that separates the Li-poor core and the Li-rich shell.[8, 81] It should be pointed out that while the strong nonlinearity of Li diffusivity is essential to produce the sharp interface, the choice of the specific functional form in Eq. (8) is only a matter of computational convenience.[66] A concentration-independent diffusivity gives rise to a diffuse-phase (single-phase) boundary. In addition, the crystallographic orientation-dependent reaction rates can be conveniently modeled by setting different values of D_0.

Numerical implementation. Aside from the in situ experimental data, atomistic simulations[37, 39, 40, 66] have been performed to

extract the material properties, including the phase-dependent moduli, the diffusivity, etc., thus fulfilling the multiscale coupling. The two sets of coupled field equations can be solved by the finite element methods. For example, the commercial package ABAQUS/Standard conveniently solves the balance equations, wherein the normalized concentration is surrogated by temperature, and the lithiation-induced volume expansion is equivalently treated as the thermal expansion. At each time step, the diffusivity and flux are updated based on the current Li concentration and stress. The increment of elastic–plastic deformation and the stress state in the electrode are then calculated according to the updated Li distribution. However, additional algorithm needs to be established to track the moving reaction front and assign appropriate orientation-dependent reaction rate (approximated by diffusivity). Another challenge for the front-tracking finite element is to maintain the sharpness of the phase boundary since its width tends to increase over time. In these regards, a phase field model may be advantageous over the discrete tracking method in finite element framework since phase field models naturally track the phase boundary with a controllable width. A recent phase field model[54] for simulating lithiation of *c*-Si demonstrated that the phase field model provides nearly equivalent results as the front-tracking finite element method.

Anisotropic swelling and fracture of *c*-Si

Several independent studies have demonstrated that *c*-Si swells anisotropically during the first lithiation, wherein <110> directions expand significantly larger than all the other directions.[7, 8, 82, 83] It was rationalized[9, 67] and experimentally verified later[81] that the anisotropic swelling arises due to the crystallographic orientation dependent lithiation rate, i.e., the chemical reaction rate is much higher along <110> directions than other directions. To simulate the anisotropic swelling of *c*-Si upon lithiation, Yang *et al*. set different lithiation rates (modeled by different diffusivity D_0 at the reaction front) at several low-index orientations,[9, 67] and interpolated the lithiation rates in other orientations by smooth functions. Combining this special treatment at the reaction front with the two sets of governing equations for Li transport and mechanical equilibrium, Yang *et al*. simulated the anisotropic cross-sectional morphologies of four *c*-SiNWs with different orientations (Fig. 3a).[9, 67] The predicted morphologies agree very well with the SEM[82] (Fig. 3b, the first three columns) and TEM[8] (Fig. 3b, the last column) images.

The orientation-dependent lithiation rate at the reaction front modulates not only the morphology of the fully lithiated Si structures, but also the subsequent fracture.[7, 8, 10] At the fastest-moving {110} interface, lithiation induces large local volumetric expansion, generating high pressure across the interface. The pressure pushes the lithiated products behind the moving interface outward.[7–9, 66, 84] The pressure and the outward pushing effect are much stronger along the <110> directions than any other directions due to the much faster lithiation rate, leading to anisotropic swelling. The lithiation-induced outward pressure generates large loop tension at the outer surface of the lithiated domain, causing surface fracture of lithiated *c*-Si. In particular, owing to the different levels of expansion along different orientations, large incompatible strains are generated at the intersections of adjacent crystalline facets near the outer surface, leading to surface crack nucleation at well-defined angular sites.[7, 8, 10] Figure 3e shows the crack nucleation sites at the outer surface of the *c*-SiNWs[71] predicted by the model, which agrees with the experimentally resolved crack nucleation sites of the four representative SiNWs upon fully lithiation[7, 8, 10] (Fig. 3d). One notes that while small-strain analysis is sufficient to predict accurate anisotropic swelling morphology of lithiated *c*-Si in Fig. 3c, finite-strain analysis is required to obtain the stress profile in Fig. 3e.

In situ TEM studies have evidenced that large *c*-SiNPs tend to be more fragile than the smaller ones, assuming other lithiation conditions (e.g., the lithiation rate) are the same, exhibiting lithiation-induced size-dependent fracture.[7, 10, 85, 86] For *c*-SiNPs there exists a critical size of ~150 nm below which lithiated *c*-SiNPs remains intact and beyond which surface fracture occurs. Many materials manifest similar size-dependent fracture, including *c*-Si, *a*-Si, *c*-Sn, etc., though the critical sizes vary for different materials. The size effect stems from the size-dependent driving force, i.e., the energy release rate, of fracture.[85] The larger the size, the higher the driving force for fracture, and the more fragile the material appears to be.

In contrast to the anisotropic swelling and surface fracture of *c*-Si, lithiation of *c*-Ge, despite its similar crystalline structures to *c*-Si and large volume expansion (~250%),[7, 87] proceeds isotropically, and the electrode remains tough without any sign of crack nucleation even for micron-sized *c*-GeNPs.[7, 88] It has been shown that *a*-Si exhibits the similar tough behavior with a critical size on the order of microns, which may similarly stem from the isotropic swelling of *a*-Si.[89, 90] These observations follow that lithiation kinetics (anisotropy, rate, etc.) modulates stress generation and fracture of the electrode materials.

Mechanical stress retards lithiation

While lithiation kinetics modulates stress generation and fracture of electrode materials, mechanical stress generated during lithiation reciprocally regulates lithiation kinetics. Lithiation generates the core-shell structures in Si and Ge: unlithiated crystalline core and lithiated amorphous shell separated by the amorphous–crystal interface (ACI, i.e., the reaction front). The incompatible strain across the ACI suggests hydrostatic stress at the ACI and possibly in the lithiated shell.[79, 87, 91] The compressive stress slows down both Li diffusivity in the lithiation shell and the reaction rate at the ACI, leading to stress-mediated lithiation retardation,[84, 92, 93] as shown in Fig. 4a. For nanosized materials, chemical reaction is the limiting step, and lithiation retardation is primarily due to the stress-reduced chemical reaction rate. In extreme cases, the compressive stress is sufficiently high to completely arrest lithiation, leaving an unlithiated core electrochemically inaccessible and resulting in a reduced capacity.

Numerical simulations have showed that lithiation anisotropy influences the distribution and level of stress generated near the ACI, which in turn yields different levels of lithiation retardation effect.[12] Figure 4b plots the thickness of the lithiated shell as a function of time, which indicates lithiation rates in three different SiNWs (*a*-SiNW, <111> *c*-SiNW, and <110> *c*-SiNW) along the specified directions (<110> direction for the *c*-SiNWs and an arbitrary direction for the *a*-SiNW). These simulations establish that the strength of the retardation effect correlates with the level of lithiation anisotropy (<110> *c*-SiNW > <111> *c*-SiNW > *a*-SiNW).

Bending force breaks the symmetry of lithiation

Similar to the self-generated mechanical stress, externally applied force also mediates lithiation kinetics. Gu *et al*. have lithiated doped *c*-GeNWs in both free-standing and externally loaded conditions.[93] For free-standing *c*-GeNWs, lithiation proceeds uniformly both in the radial and longitudinal directions. In the externally loaded condition, the *c*-GeNWs were pushed sideway against the counter electrode (Li metal) while being lithiated. In addition to axial compression, the pushing generates bending force that locally curves the *c*-GeNWs. This results in stress asymmetry in the curved region: tensile stress on one side and compressive stress on the other. As tensile stress promotes lithiation and compressive stress suppresses it, the stress asymmetry leads to lithiation asymmetry. Indeed, in situ TEM imaging observed that the lithiated shell on the tensile side of the curved region is several fold thicker than the compressive side

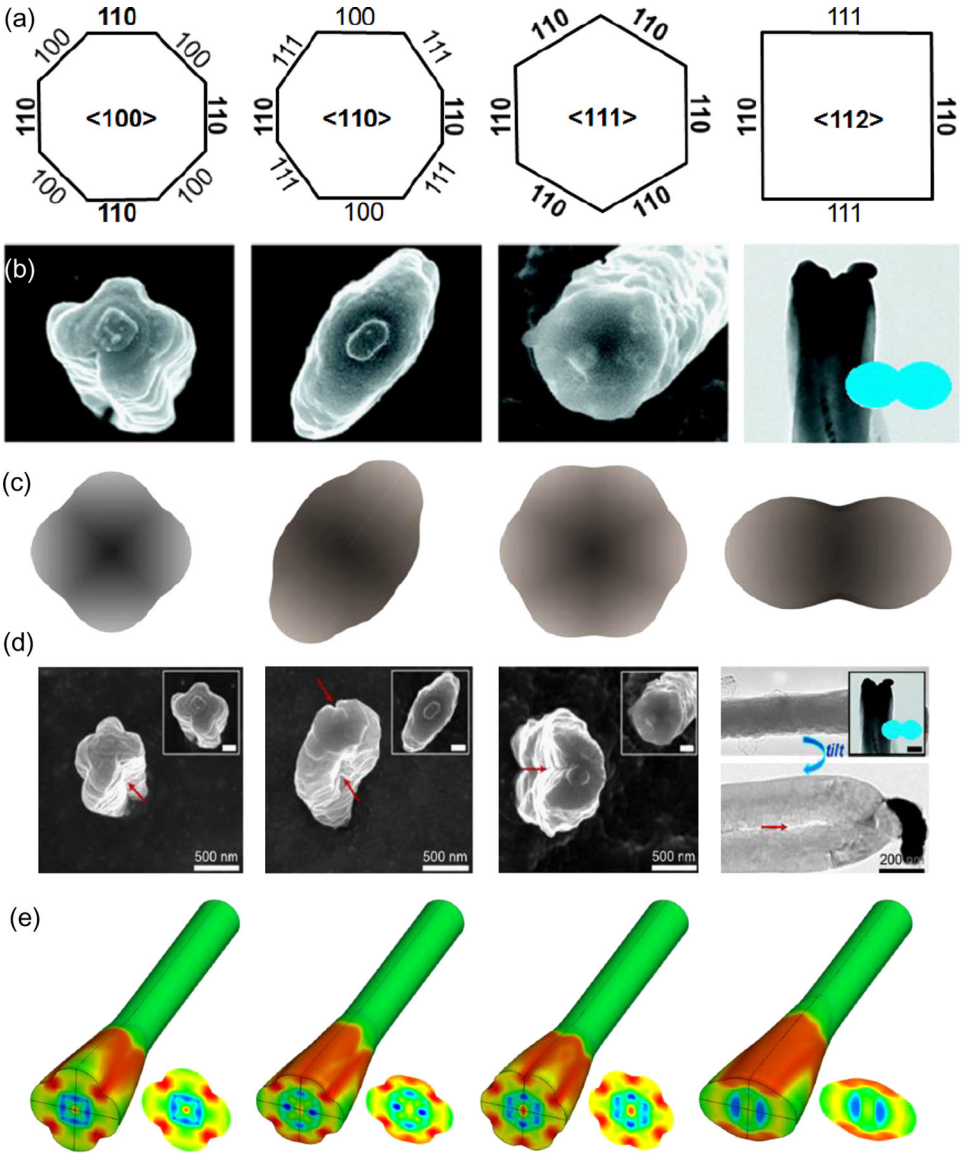

Fig. 3 Lithiation-induced anisotropic swelling and fracture in *c*-Si. **a** Four *c*-SiNWs with different crystallographic orientations. Indices in the center represent the axial orientation, while those on the sides the orientations of the facets. **b** SEM[82] (the first three columns) and TEM[8] (the last column) images of a fully lithiated *c*-SiNWs, displaying different cross-sectional morphologies with clear swelling anisotropy. **c** Anisotropic cross-sectional morphologies of lithiated *c*-SiNWs corresponding to the orientations shown in (**a**), predicted by the front-tracking finite element modeling.[9, 67] **d** SEM[82] (the first three columns) and TEM[8] (the last column) images showing the crack nucleation sites (marked by *red arrows*) in the lithiated *c*-SiNWs of four different orientations (**a**). **e** Stress concentration locations (*red spots*) predicted by 3D front-tracking finite element modeling[63] coincide with the experimentally observed crack nucleation sites

(Fig. 5a), demonstrating bending-induced symmetry breaking in lithiation. Front-tracking finite element modeling shows that the symmetry breaking occurs not only in the longitudinal direction, but also in the radial direction close to the bending site[93] (Fig. 5b). The lithiation morphology aligns with the mechanical stress distribution (Fig. 5c), demonstrating the role of mechanical stress on the lithiation kinetics and morphology.

FROM ELECTROCHEMICAL-MECHANICS COUPLING TO MECHANICAL ENERGY HARVESTING

The kinetics–stress coupling in lithiation has inspired electrochemically driven mechanical energy harvesting. Kim *et al.*[94] developed a prototype mechanical energy harvester (Fig. 6a), consisting of two identical electrodes sandwiching a separator soaked with electrolyte.[94] Amorphous prelithiated Si (Li_xSi, $x \sim 3.1$) thin films were used as the electrodes for its mechanical flexibility and reasonable lithiation and delithiation rates. Ethylene carbonate mixed with ethyl methyl carbonate, $LiPF_6$ and micro-porous polypropylene monolayer[95] were used as the electrolyte, Li salt and separator, respectively. Each Li_xSi electrode is 250 nm thick, two orders of magnitude thinner than the separator layer (25 μm). The thin-film configuration of the device allows large-curvature bending without fatigue.

Figure 6b schematically illustrates the working principle of the energy harvester, consisting of two partially prelithiated electrodes (*eucalyptus*) sandwiching an electrolyte (*gray*). The electrodes are adhered to cupper foils as the current collectors (*gold*). Starting from the initial stress-free condition (I in Fig. 5b), Li concentrations in the two prelithiated electrodes are the same (denoted by the

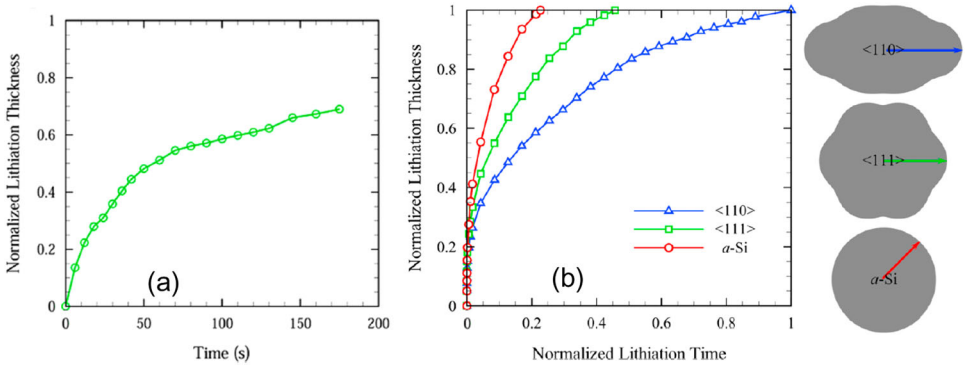

Fig. 4 Lithiation retardation in GeNWs. **a** The plot of the thickness of lithiated shell (normalized by the thickness of the pristine GeNW) as a function of the lithiation time shows lithaition rate decreases with time. **b** The retardation effect is stronger with stronger lithiation anisotropy. The lithiation dynamics is measured along <110> directions in the *c*-SiNWs and an arbitrary direction in the *a*-SiNW[12]

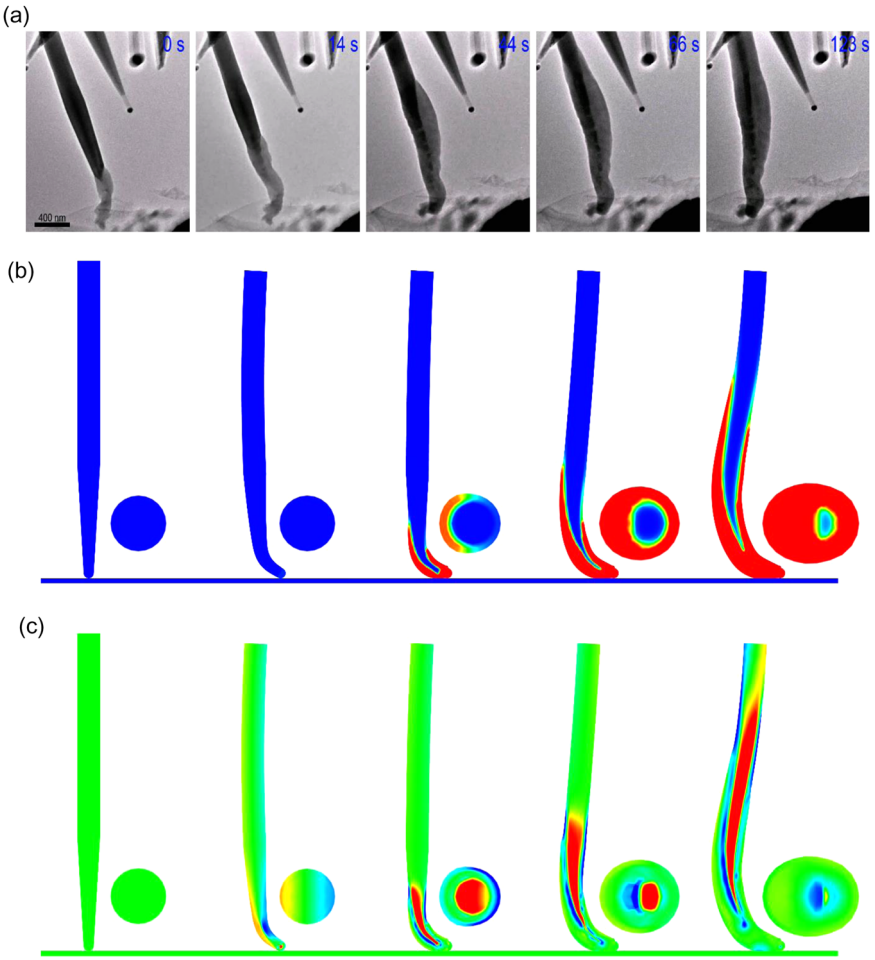

Fig. 5 External bending force breaks the lithiation symmetry in *c*-GeNWs.[93] **a** Time-elapsed TEM images show symmetry breaking of lithiation in a *c*-GeNW with applied bending force. A comparison of the lithiated thickness showed that lithiation proceeded appreciably faster along the tensile side than the compressive side. Li metal at the bottom of the image serves as the counter electrode and Li source. **b** Chemomechanical modeling of the symmetry breaking in a bent *c*-GeNW. The symmetry breaking occurs both in the longitudinal and radial directions of the nanowire. *Blue*: unlithiated region, *red*: lithiated region, transition color: ACI. *Bottom blue* substrate represents Li metal. **c** Mechanical stress evolution during the lithiation, corresponding to the lithiation kinetics shown in **b**. *Red*: tension, *blue*: compression

same color) and thus they are isopotential. Bending the thin film device generates net tension in the bottom electrode and compression in the top (II). The stress difference creates a chemical potential difference, driving Li ions migration from the compressed to the tensed electrode through the electrolyte (II-III). The Li ion migration continues until the chemical potential difference vanishes (III), establishing a new equilibrium state on the two electrodes with different Li concentration (see the color difference in the two electrodes, *eucalyptus* and *cyan*, representing different Li concentrations). This new equilibrium state is set by

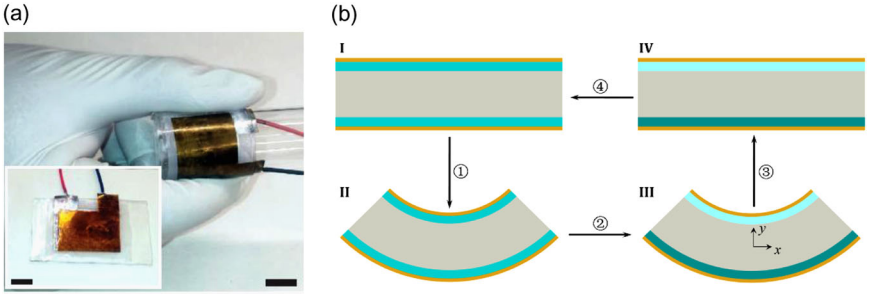

Fig. 6 **a** An image of the actual device with a bending unit.[94] Scale bars: 1 cm. **b** Schematic illustrating working principle of the mechanical energy harvester (*gold*: current collector, *eucalyptus*: electrode with high Li concentration, *cyan*: electrode with low Li concentration, *gray*: electrolyte)

the counteractions between the Li concentration gradient and the stress gradient. Removing the curvature (III-IV) releases the stress and hence breaks the chemical equilibrium. As a result, the chemical potential difference of Li is solely caused by Li concentration gradient, driving Li ion migration in the opposite direction (IV-I), thus discharging the device. To maintain charge neutrality, electrons flow in the outer circuit, generating electrical power. The device goes back to its original equilibrium state and can bend back and forth for thousands of cycles provided that it operates in the viscoelastic regime without any irreversible damage.[94]

STRATEGIES FOR MITIGATING THE ELECTROCHEMO-MECHANICAL DEGRADATION

To improve electrochemical performance of high-capacity LIBs, different design strategies have been undertaken to mitigate the chemomechanical degradation of the high-capacity electrode materials. In light of the size-dependent fracture behavior of *c*-Si, using nanoscale materials becomes a logic route to mitigating degradation. The large surface-to-volume ratio of nanoscale materials, such as nanowires, nanoparticles, nanotubes, and nanothick thin films, facilitate stress relaxation and enhance flaw tolerance, and is thus tougher than their bulk counterparts.[4] The shortened ion and electron diffusion paths and increased surface area of the electrodes for fast chemical reactions[4, 96, 97] of nanosized structures also enhance the rate performance. Material compositing, wherein one material component (e.g., Si) is used to store Li, and the other (e.g., carbon) to enhance the overall conductivity and mechanical stability,[61, 98–101] has also been adopted to improve the electrochemical performance of the electrode materials.

In addition to nanostructuring and nanocompositing, porous materials have become popular method to mitigate the degradation of high-energy-density electrode materials.[44, 102–107] Porous materials can provide large surface areas for reaction, interconnected and fast interfacial transport, and hence enhanced rate performance. The internal pores can accommodate volume changes and alleviate mechanical stress generation during lithiation/delithiation cycles, thereby improving the structural stability and durability.

Porous materials exhibit different deformation modes than their solid counterparts, as schematically shown in Fig. 7a, b. During lithiation of solid Si or Ge, newly lithiated product at the reaction front pushes both the lithiated shell and unlithiated core to relax the high strain energy. As the lithiated product in the lithiated shell ($Li_{3.75}Si$ or $Li_{3.75}Ge$) possess a relatively lower stiffness and lower flow stress than those of the unlithiated core, the reaction front pushes outward much more than inward, giving rise to outward expansion of the lithiated Si.[7, 8, 80, 82, 89] As a result, large hoop tension is generated in the lithiated outer shell, causing surface fracture, as already shown in Fig. 7c, d. In contrast, the presence of porosity alters the deformation mode since the volume change due to lithiation/delithiation can be partially accommodated by the pore filling and formation. In essence, the pressure generated at the reaction front may push both outward the lithiated shell and inward the unlithiated core, giving rise to less apparent particle-level expansion. This helps stabilize the SEI layer and maintain materials/structural stability.

A recent work by Xiao *et al.*[44] showed that hierarchically porous SiNPs (hp-SiNPs) can reverse the deformation mode seen in lithiated solid Si. The hp-SiNP, about 400 nm in diameter, consists of a hollow core and a porous shell. During lithiation, the filling effect of Li to the pores renders a stiffer lithiated shell than the unlithiated core. As a result, the compressive stress generated at the reaction front pushes more inward than outward, resulting negligible outward expansion (Fig. 7e, f). During delithiation, the generated tensile stress across the Li-poor outer layer to the Li-rich inner layer pulls the inner layer outward (Fig. 7g, h). This deformation mode in each lithiation/delithiation cycle features Li breathing of the particle, with negligible exterior volume expansion, i.e., the apparent size of the hierarchically structured porous material remains nearly unchanged during the cycling. Tailoring materials and structural properties and electrochemical parameters to obtain such hierarchically structured porous materials represents a new avenue to mitigate battery degradation.

Surface coating acts as a multiple functional layer that mitigates chemomechanical degradation. First, surface coating constrains the volumetric change during electrochemical cycling, preventing the cracking and pulverization of high-capacity electrodes.

Some coating materials, such as Al_2O_3,[43, 108, 109] function as a passivation layer, which suppresses unwanted chemical reactions between electrodes and electrolytes, and subsequently prevents wasting Li sources in the electrolyte. Conductive coatings such as carbon,[110–120] metals,[121–123] and conductive polymers[43, 124–127] can enhance the redox reaction kinetics and improve the current collection efficiency. Surface coatings can also prevent electrochemical welding between particles of active materials.[128, 129]

In uncoated Si, lithiation generated compressive stress at the reaction front and in the *a*-Li_xSi phase, slows down the reaction and Li diffusion, causing lithiation retardation. In the presence of surface coating, the constraint of the coating may cause even high compressive stress inside the SiNP as the SiNP swells,[112, 116] which modifies the driving force both for chemical reaction at the reaction front and the diffusion behind, as shown in a comparative study for pure Si and Si coated with elastic coating in Fig. 8. The level of buildup compressive stress in Si depends on the elastic properties of the coating and the lithiation thickness. For highly flexible coating (polymer), the large volume expansion can be accommodated by the coating without significant energy cost, giving rise to relatively low compressive stress, and insignificant retardation effect.[43] For rigid coatings (carbon or native oxide),

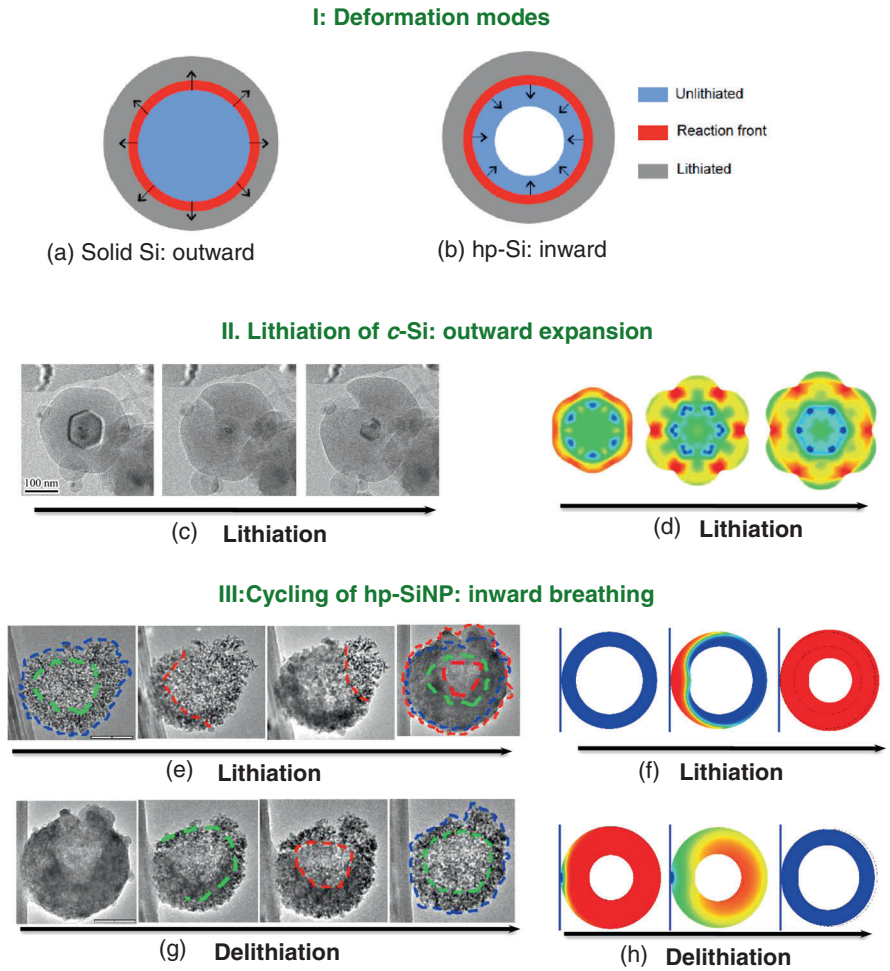

Fig. 7 **I** Different deformation modes of solid SiNP and hp-SiNP during lithiation/delithiation cycles. **a** When lithiating solid Si (*c*-Si or *a*-Si), the reaction front (*red*) pushes outward more than inward because the unlithiated core (*light blue*) is much stiffer than the lithiated shell (*gray*). **b** When lithiating hp-SiNP with a hollow center (*white*), the reaction front pushes inward much more than outward because the lithiated shell (*gray*) is stiffer than the unlithiated porous core (*light blue*). **II** Lithiation of *c*-SiNP causes anisotropic outward expansion, generates large hoop tension in the lithiated shell, leading to surface fracture. **c** Time-lapse TEM images showing the lithiation-induced fracture process of a *c*-SiNP.[7] **d** Front-tracking simulations show the development of stress concentration at the outer surface of the lithiated SiNP, indicating fracture and possible fracture sites.[63] **III** Inward Li breathing of hp-SiNPs.[44] **e**, **g** Time-lapse TEM images of the first lithiation (**e**) and delithiation (**g**) of a hp-SiNP (Scale bar: 200 nm). *Blue* and *green dashed lines* are the outer and inner surface profiles of the hp-SiNP prior to lithiation, and the *red dashed line* marks the lithiation and delithiation front. The images show that the lithiated hp-SiNP returns nearly to its original size (both inner and outer radii), demonstrating inward Li breathing and its high reversibility upon electrochemical cycling. **f**–**h** Chemomechanical modeling of a hp-SiNP shows that volume changes during lithiation (**f**) and delithiation (**h**) cycling are accommodated largely by inward Li breathing, causing negligible exterior volume change. Colors denote Li concentration. *Red*: fully lithiated, *blue*: unlithiated

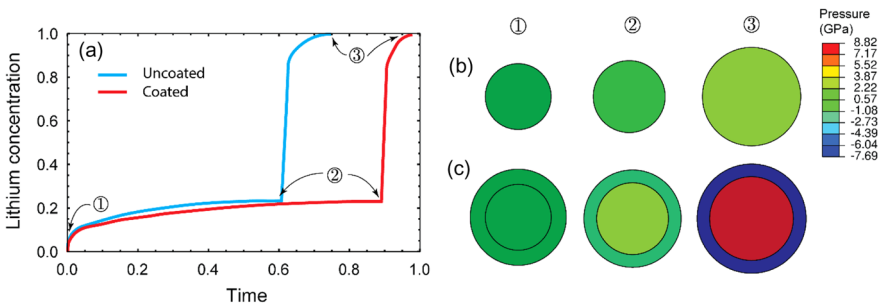

Fig. 8 The Li concentration at the lithiation front indicates different lithiation retardation in uncoated and coated SnNPs. Sn (Tin) features a two-step lithiation mechanism. The first step proceeds by two-phase lithiation with a sharp interface with a product of *a*-LiSn. The second step proceeds by single-phase lithiation. **a** The lithiation front tracked by the lithiation concentration with time. Coated SnNP features a stronger retardation than uncoated SnNP. The different lithiation retardation behavior corresponds to the stress generation at different lithiation stages (indicated in (**a**)) for the uncoated (**b**) and coated (**c**) SnNPs

very large compressive stress may be built up before the coating fractures, causing significant lithiation retardation. As a result, a large amount of the Si core may not be electrochemically accessible. This reduces the effective capacity.

In battery cells, the electrodes consist of particle aggregates. During lithiation/delithiation cycles, neighboring particles interact not only mechanically but also kinetically, and these two interactions are intimately coupled. For the uncoated SiNPs, the hydrostatic stress at the outer surfaces of the uncoated bare SiNPs is the same regardless of the particle size and lithiation depth. This follows that the Li chemical potential at the outer surface is the same throughout the lithiation process and neighboring bare SiNPs are lithiated without kinetic interactions. In contrast, the stress-mediated Li chemical potential at the outer surface of coated SiNPs depends on the initial SiNP size, lithiation thickness, and the mechanical stress. When two coated SiNPs are in contact, the difference of the Li chemical potential caused by any of the factors drive inter-SiNP Li diffusion,[127] leading to discharging in one SiNPs, and charging in the other. This inter-SiNP Li diffusion dynamically occurs at different stages of lithiation, possibly impact the lithiation kinetics.

CONCLUSIONS AND PERSPECTIVES

Combined experimental and modeling studies have demonstrated that the strong coupling between electrochemistry and mechanics dictates the degradation of high-capacity electrode materials. On the one hand, electrochemical lithiation causes volume expansion and mechanical stress generation; on the other, mechanical stress retards or even arrests lithiation. The ubiquitous coupling sets capacity and cyclability as the two conflicting properties since improving one often compromises the other, creating a significant challenge in the design of high-performance LIBs. While sodium ion batteries are not reviewed here, such electrochemistry-mechanics coupling also exists and is probably even stronger since the mechanical stress generated by sodiation is higher due to the much larger size of the sodium ions. On the opposite side, we have shown that the coupling phenomena can be exploited for electrochemically driven mechanical energy harvesting.

With the in situ TEM imaging and multiphysical modeling, much is known as to the pulverization and fracture of various electrode materials on the single particle level, ranging from anisotropic swelling and fracture of *c*-Si during the first lithiation, the tough behavior of *c*-Ge and *a*-Si, etc. In contrast, delithiation-induced morphological change and its implications to the successive lithiation cycles are much less understood. For examples, nanopore formation seems to be a ubiquitous phenomenon during delithiation.[7, 130–133] Yet little is known as to how the pore structures evolve upon multiple cycling and how these pore structures modify the cycling performance of the electrode materials. In addition, while it is clear that unstable SEI growth critically limits the cyclability of the LIBs, it remains a challenge to in situ imaging with atomic resolution and modeling the growth process of the SEI layer.

Electrochemical cycling is rich in interfacial processes that directly modulate battery degradation. For examples, SEI formation and dendrite growth of Li are regulated by the electrode–electrolyte interface;[134–136] stress generation and failure of the electrode materials depends on the motion and morphology of the reaction front. The correlation of the interlayer process and the degradation has motivated fundamental understanding of the interfacial processes on the one hand, and tailoring and modifying the interfaces as ways to mitigate degradation on the other. In the future, focused studies are still critically needed to understand and control these interfacial processes to enhance the overall performance of the electrode materials for LIBs.

ACKNOWLEDGEMENTS

S.Z. acknowledges the support by the National Science Foundation through the projects CMMI-0900692, DMR-1610430, and ECCS-1610331.

COMPETING INTERESTS

The authors declare that they have no competing interests.

REFERENCES

1. Beaulieu, L. Y., Eberman, K. W., Turner, R. L., Krause, L. J. & Dahn, J. R. Colossal reversible volume changes in lithium alloys. *Electrochem. Solid State Lett.* **4**, A137–A140 (2001).
2. Limthongkul, P., Jang, Y.-I., Dudney, N. J. & Chiang, Y.-M. Electrochemically-driven solid-state amorphization in lithium-silicon alloys and implications for lithium storage. *Acta Mater.* **51**, 1103–1113 (2003).
3. Graetz, J., Ahn, C. C., Yazami, R. & Fultz, B. Nanocrystalline and thin film germanium electrodes with high lithium capacity and high rate capabilities. *J. Electrochem. Soc.* **151**, A698–A702 (2004).
4. Chan, C. K., Patel, R. N., O'Connell, M. J., Korgel, B. A. & Cui, Y. Solution-grown silicon nanowires for lithium-ion battery anodes. *ACS Nano* **4**, 1443–1450 (2010).
5. Chan, C. K. *et al.* High-performance lithium battery anodes using silicon nanowires. *Nat. Nanotechnol* **3**, 31–35 (2008).
6. Chan, C. K., Zhang, X. F. & Cui, Y. High capacity Li ion battery anodes using Ge nanowires. *Nano Lett.* **8**, 307–309 (2008).
7. Liang, W. *et al.* Tough germanium nanoparticles under electrochemical cycling. *ACS Nano* **7**, 3427–3433 (2013).
8. Liu, X. H. *et al.* Anisotropic swelling and fracture of silicon nanowires during lithiation. *Nano Lett.* **11**, 3312–3318 (2011).
9. Yang, H. *et al.* Orientation-dependent interfacial mobility governs the anisotropic swelling in lithiated silicon nanowires. *Nano Lett.* **12**, 1953–1958 (2012).
10. Lee, S. W., McDowell, M. T., Berla, L. A., Nix, W. D. & Cui, Y. Fracture of crystalline silicon nanopillars during electrochemical lithium insertion. *Proc. Natl. Acad. Sci. USA* **109**, 4080–4085 (2012).
11. Ryu, I., Lee, S. W., Gao, H., Cui, Y. & Nix, W. D. Microscopic model for fracture of crystalline Si nanopillars during lithiation. *J. Power Sources* **255**, 274–282 (2014).
12. Yang, H., Liang, W., Guo, X., Wang, C. & Zhang, S. Strong kinetics-stress coupling in lithiated Si and Ge electrodes. *Extreme Mech. Lett.* **2**, 1–6 (2015).
13. Wu, H. *et al.* Stable cycling of double-walled silicon nanotube battery anodes through solid-electrolyte interphase control. *Nat. Nanotechnol* **7**, 309–314 (2012).
14. Hertzberg, B., Benson, J. & Yushin, G. Ex-situ depth-sensing indentation measurements of electrochemically produced Si–Li alloy films. *Electrochem. Commun.* **13**, 818–821 (2011).
15. Berla, L. A., Lee, S. W., Cui, Y. & Nix, W. D. Mechanical behavior of electrochemically lithiated silicon. *J. Power Sources* **273**, 41–51 (2015).
16. de Vasconcelos, L. S., Xu, R., Li, J. & Zhao, K. Grid indentation analysis of mechanical properties of composite electrodes in Li-ion batteries. *Extreme Mech. Lett.* **9**, 495–502 (2016).
17. Pyun, S.-I., Go, J.-Y. & Jang, T.-S. An investigation of intercalation-induced stresses generated during lithium transport through Li 1− δ CoO 2 film electrode using a laser beam deflection method. *Electrochim. Acta* **49**, 4477–4486 (2004).
18. Kim, Y.-H., Pyun, S.-I. & Go, J.-Y. An investigation of intercalation-induced stresses generated during lithium transport through sol–gel derived Li x Mn 2 O 4 film electrode using a laser beam deflection method. *Electrochim. Acta* **51**, 441–449 (2005).
19. Sethuraman, V. A., Chon, M. J., Shimshak, M., Srinivasan, V. & Guduru, P. R. In situ measurements of stress evolution in silicon thin films during electrochemical lithiation and delithiation. *J. Power Sources* **195**, 5062–5066 (2010).
20. Sethuraman, V. A., Srinivasan, V., Bower, A. F. & Guduru, P. R. In situ measurements of stress-potential coupling in lithiated silicon. *J. Electrochem. Soc.* **157**, A1253–A1261 (2010).
21. Pharr, M., Suo, Z. & Vlassak, J. J. Measurements of the fracture energy of lithiated silicon electrodes of Li-ion batteries. *Nano Lett.* **13**, 5570–5577 (2013).
22. Choi, Y. S., Pharr, M., Oh, K. H. & Vlassak, J. J. A simple technique for measuring the fracture energy of lithiated thin-film silicon electrodes at various lithium concentrations. *J. Power Sources* **294**, 159–166 (2015).
23. Pharr, M., Choi, Y. S., Lee, D., Oh, K. H. & Vlassak, J. J. Measurements of stress and fracture in germanium electrodes of lithium-ion batteries during electrochemical lithiation and delithiation. *J. Power Sources* **304**, 164–169 (2016).
24. Huang, J. Y. *et al.* In situ observation of the electrochemical lithiation of a single sno2 nanowire electrode. *Science* **330**, 1515–1520 (2010).

25. Kubota, Y., Escano, M. C. S., Nakanishi, H. & Kasai, H. Crystal and electronic structure of Li15Si4. *J. Appl. Phys.* **102**, 053704 (2007).
26. Kubota, Y., Escano, M. C. S., Nakanishi, H. & Kasai, H. Electronic structure of LiSi. *J. Alloys. Compd.* **458**, 151–157 (2008).
27. Chevrier, V. L. & Dahn, J. R. First principles model of amorphous silicon lithiation. *J. Electrochem. Soc.* **156**, A454–A458 (2009).
28. Chevrier, V. L. & Dahn, J. R. First principles studies of disordered lithiated silicon. *J. Electrochem. Soc.* **157**, A392–A398 (2010).
29. Shenoy, V. B., Johari, P. & Qi, Y. Elastic softening of amorphous and crystalline Li-Si Phases with increasing Li concentration: a first-principles study. *J. Power Sources* **195**, 6825–6830 (2010).
30. Zhang, Q. F., Zhang, W. X., Wan, W. H., Cui, Y. & Wang, E. G. Lithium insertion in silicon nanowires: an ab initio study. *Nano Lett.* **10**, 3243–3249 (2010).
31. Wan, W. H., Zhang, Q. F., Cui, Y. & Wang, E. G. First principles study of lithium insertion in bulk silicon. *J. Phys. Condens. Matter* **22**, 415501 (2010).
32. Zhang, Q., Cui, Y. & Wang, E. Anisotropic lithium insertion behavior in silicon nanowires: binding energy, diffusion barrier, and strain effect. *J. Phys. Chem. C* **115**, 9376–9381 (2011).
33. Chevrier, V. L., Zwanziger, J. W. & Dahn, J. R. First principles studies of silicon as a negative electrode material for lithium-ion batteries. *Can. J. Phys.* **87**, 625–632 (2009).
34. Kim, H., Kweon, K. E., Chou, C.-Y., Ekerdt, J. G. & Hwang, G. S. On the nature and behavior of Li Atoms in Si: a first principles study. *J. Phys. Chem. C* **114**, 17942–17946 (2010).
35. Zhao, K. *et al.* Lithium-assisted plastic deformation of silicon electrodes in lithium-ion batteries: a first-principles theoretical study. *Nano Lett.* **11**, 2962–2967 (2011).
36. Urban, A., Seo, D.-H. & Ceder, G. Computational understanding of Li-ion batteries. *NPJ Comput. Mater.* **2**, 16002 (2016).
37. Yang, H. *et al.* Self-weakening in lithiated graphene electrodes. *Chem. Phys. Lett.* **563**, 58–62 (2013).
38. Huang, X. *et al.* Lithiation induced corrosive fracture in defective carbon nanotubes. *Appl. Phys. Lett.* **103**, 153901–153904 (2013).
39. Fan, F. *et al.* Mechanical properties of amorphous LixSi alloys: a reactive force field study. *Model. Simul. Mater. Sci. Eng.* **21**, 047002 (2013).
40. Ostadhossein, A. *et al.* Stress effects on the initial lithiation of crystalline silicon nanowires: reactive molecular dynamics simulations using ReaxFF. *Phys. Chem. Chem. Phys.* **17**, 3832–3840 (2015).
41. Chew, H. B., Hou, B. Y., Wang, X. J. & Xia, S. M. Cracking mechanisms in lithiated silicon thin film electrodes. *Int. J. Solids Struct.* **51**, 4176–4187 (2014).
42. Zhang, S. L., Zhu, T. & Belytschko, T. Atomistic and multiscale analyses of brittle fracture in crystal lattices. *Phys. Rev. B* **76**, 094114 (2007).
43. Luo, L. L. *et al.* Surface-coating regulated lithiation kinetics and degradation in silicon nanowires for lithium ion battery. *ACS Nano* **9**, 5559–5566 (2015).
44. Xiao, Q. *et al.* Inward lithium-ion breathing of hierarchically porous silicon anodes. *Nat. Commun.* **6**, 8844 (2015).
45. Bhandakkar, T. K. & Gao, H. J. Cohesive modeling of crack nucleation under diffusion induced stresses in a thin strip: Implications on the critical size for flaw tolerant battery electrodes. *Int. J. Solids Struct.* **47**, 1424–1434 (2010).
46. Christensen, J. & Newman, J. Stress generation and fracture in lithium insertion materials. *J. Solid State Electrochem.* **10**, 293–319 (2006).
47. Zhang, X. C., Shyy, W. & Sastry, A. M. Numerical simulation of intercalation-induced stress in Li-ion battery electrode particles. *J. Electrochem. Soc.* **154**, A910–A916 (2007).
48. Deshpande, R., Cheng, Y. T. & Verbrugge, M. W. Modeling diffusion-induced stress in nanowire electrode structures. *J. Power Sources* **195**, 5081–5088 (2010).
49. Woodford, W. H., Chiang, Y. M. & Carter, W. C. "Electrochemical shock" of intercalation electrodes: a fracture mechanics analysis. *J. Electrochem. Soc.* **157**, A1052–A1059 (2010).
50. Chandrasekaran, R., Magasinski, A., Yushin, G. & Fuller, T. F. Analysis of lithium insertion/deinsertion in a silicon electrode particle at room temperature. *J. Electrochem. Soc.* **157**, A1139–A1151 (2010).
51. Gao, Y. F. & Zhou, M. Strong stress-enhanced diffusion in amorphous lithium alloy nanowire electrodes. *J. Appl. Phys.* **109**, 014310 (2011).
52. Bucci, G., Nadimpalli, S. P. V., Sethuraman, V. A., Bower, A. F. & Guduru, P. R. Measurement and modeling of the mechanical and electrochemical response of amorphous Si thin film electrodes during cyclic lithiation. *J. Mech. Phys. Solids* **62**, 276–294 (2014).
53. Nadimpalli, S. P. V. *et al.* Quantifying capacity loss due to solid-electrolyte-interphase layer formation on silicon negative electrodes in lithium-ion batteries. *J. Power Sources* **215**, 145–151 (2012).
54. Chen, L. *et al.* A phase-field model coupled with large elasto-plastic deformation: application to lithiated silicon electrodes. *J. Electrochem. Soc.* **161**, F3164–F3172 (2014).
55. Jia, Z. & Li, T. Failure mechanics of a wrinkling thin film anode on a substrate under cyclic charging and discharging. *Ext. Mech. Lett.* **8**, 273–282 (2016).
56. Huggins, R. *Advanced Batteries: Materials Science Aspects*. (Springer, 2008).
57. Liu, X. H. *et al.* In situ transmission electron microscopy of electrochemical lithiation, delithiation and deformation of individual graphene nanoribbons. *Carbon* **50**, 3836–3844 (2012).
58. Liu, Y. *et al.* Lithiation-induced embrittlement of multiwalled carbon nanotubes. *ACS Nano* **5**, 7245–7253 (2011).
59. Kamali, A. R. & Fray, D. J. Review on carbon and silicon based materials as anode materials for lithium ion batteries. *J. New Mater. Electrochem. Syst.* **13**, 147–160 (2010).
60. Tarascon, J. M. & Armand, M. Issues and challenges facing rechargeable lithium batteries. *Nature* **414**, 359–367 (2001).
61. Zhang, W. J. A review of the electrochemical performance of alloy anodes for lithium-ion batteries. *J. Power Sources* **196**, 13–24 (2011).
62. Marom, R., Amalraj, S. F., Leifer, N., Jacob, D. & Aurbach, D. A review of advanced and practical lithium battery materials. *J. Mater. Chem.* **21**, 9938–9954 (2011).
63. Neumann, G. & Würsig, A. Lithium storage in silicon. *Phys. Status Solidi Rapid Res. Lett.* **4**, A21–A23 (2010).
64. Grantab, R. & Shenoy, V. B. Pressure-gradient dependent diffusion and crack propagation in lithiated silicon nanowires. *J. Electrochem. Soc.* **159**, A584–A591 (2012).
65. Sheldon, B. W., Soni, S. K., Xiao, X. C. & Qi, Y. Stress contributions to solution thermodynamics in Li-Si alloys. *Electrochem. Solid State Lett.* **15**, A9–A11 (2012).
66. Huang, S., Fan, F., Li, J., Zhang, S. & Zhu, T. Stress generation during lithiation of high-capacity electrode particles in lithium ion batteries. *Acta Mater.* **61**, 4354–4364 (2013).
67. Yang, H. *et al.* A chemo-mechanical model of lithiation in silicon. *J. Mech. Phys. Solids* **70**, 349–361 (2014).
68. Zhao, K. J., Pharr, M., Vlassak, J. J. & Suo, Z. G. Inelastic hosts as electrodes for high-capacity lithium-ion batteries. *J. Appl. Phys.* **109**, 016110 (2011).
69. Bower, A. *Applied Mechanics of Solids*. (CRC Press, 2010).
70. Bower, A. F. & Guduru, P. R. A simple finite element model of diffusion, finite deformation, plasticity and fracture in lithium ion insertion electrode materials. *Model. Simul. Mater. Sci. Eng.* **20**, 045004 (2012).
71. Gao, Y. F. & Zhou, M. Strong dependency of lithium diffusion on mechanical constraints in high-capacity Li-ion battery electrodes. *Acta Mech. Sin.* **28**, 1068–1077 (2012).
72. Gao, Y. F. & Zhou, M. Coupled mechano-diffusional driving forces for fracture in electrode materials. *J. Power Sources* **230**, 176–193 (2013).
73. Cui, Z. W., Gao, F. & Qu, J. M. A finite deformation stress-dependent chemical potential and its applications to lithium ion batteries. *J. Mech. Phys. Solids* **60**, 1280–1295 (2012).
74. Khosrownejad, S. M. & Curtin, W. A. Model for charge/discharge-rate-dependent plastic flow in amorphous battery materials. *J. Mech. Phys. Solids* **94**, 167–180 (2016).
75. Zhao, K. J. *et al.* Reactive flow in silicon electrodes assisted by the insertion of lithium. *Nano Lett.* **12**, 4397–4403 (2012).
76. Jia, Z. & Liu, W. K. Rate-dependent stress evolution in nanostructured Si anodes upon lithiation. *Appl. Phys. Lett.* **109**, 163903 (2016).
77. Pharr, M., Suo, Z. G. & Vlassak, J. J. Variation of stress with charging rate due to strain-rate sensitivity of silicon electrodes of Li-ion batteries. *J. Power Sources* **270**, 569–575 (2014).
78. Chon, M. J., Sethuraman, V. A., McCormick, A., Srinivasan, V. & Guduru, P. R. Real-time measurement of stress and damage evolution during initial lithiation of crystalline silicon. *Phys. Rev. Lett.* **107**, 4 (2011).
79. Wang, J. W. *et al.* Two-phase electrochemical lithiation in amorphous silicon. *Nano Lett.* **13**, 709–715 (2013).
80. McDowell, M. T. *et al.* In situ TEM of two-phase lithiation of amorphous silicon nanospheres. *Nano Lett.* **13**, 758–764 (2013).
81. Liu, X. H. *et al.* In situ atomic-scale imaging of electrochemical lithiation in silicon. *Nat. Nanotechnol.* **7**, 749–756 (2012).
82. Lee, S. W., McDowell, M. T., Choi, J. W. & Cui, Y. Anomalous shape changes of silicon nanopillars by electrochemical lithiation. *Nano Lett.* **11**, 3034–3039 (2011).
83. Goldman, J. L., Long, B. R., Gewirth, A. A. & Nuzzo, R. G. Strain anisotropies and self-limiting capacities in single-crystalline 3D silicon microstructures: models for high energy density lithium-ion battery anodes. *Adv. Funct. Mater.* **21**, 2412–2422 (2011).
84. McDowell, M. T. *et al.* Studying the kinetics of crystalline silicon nanoparticle lithiation with in situ transmission electron microscopy. *Adv. Mater.* **24**, 6034–6041 (2012).
85. Liu, X. H. *et al.* Size-dependent fracture of silicon nanoparticles during lithiation. *ACS Nano* **6**, 1522–1531 (2012).
86. Ryu, I., Choi, J. W., Cui, Y. & Nix, W. D. Size-dependent fracture of Si nanowire battery anodes. *J. Mech. Phys. Solids* **59**, 1717–1730 (2011).
87. Liu, X. H. *et al.* In situ TEM experiments of electrochemical lithiation and delithiation of individual nanostructures. *Adv. Energy Mater* **2**, 722–741 (2012).

88. Lee, S. W., Ryu, I., Nix, W. D. & Cui, Y. Fracture of crystalline germanium during electrochemical lithium insertion. *Extreme Mech. Lett* **2**, 15–19 (2015).
89. Berla, L. A., Lee, S. W., Ryu, I., Cui, Y. & Nix, W. D. Robustness of amorphous silicon during the initial lithiation/delithiation cycle. *J. Power Sources* **258**, 253–259 (2014).
90. Jia, Z. & Li, T. Intrinsic stress mitigation via elastic softening during two-step electrochemical lithiation of amorphous silicon. *J. Mech. Phys. Solids* **91**, 278–290 (2016).
91. Liu, Y., Zhang, S. & Zhu, T. Germanium-based electrode materials for lithium-ion batteries. *ChemElectroChem* **1**, 706–713 (2014).
92. Liu, X. H. *et al.* Self-limiting lithiation in silicon nanowires. *ACS Nano* **7**, 1495–1503 (2013).
93. Gu, M. *et al.* Bending-induced symmetry breaking of lithiation in germanium nanowires. *Nano Lett.* **14**, 4622–4627 (2014).
94. Kim, S. *et al.* Electrochemically driven mechanical energy harvesting. *Nat. Commun.* **7**, 10146 (2016).
95. Cannarella, J. *et al.* Mechanical properties of a battery separator under compression and tension. *J. Electrochem. Soc.* **161**, F3117–F3122 (2014).
96. Szczech, J. R. & Jin, S. Nanostructured silicon for high capacity lithium battery anodes. *Energy Environ. Sci.* **4**, 56–72 (2011).
97. Cui, L. F., Hu, L. B., Choi, J. W. & Cui, Y. Light-weight free-standing carbon nanotube-silicon films for anodes of lithium ion batteries. *ACS Nano* **4**, 3671–3678 (2010).
98. Sun, C. F. *et al.* A beaded-string silicon anode. *ACS Nano* **7**, 2717–2724 (2013).
99. Kasavajjula, U., Wang, C. & Appleby, A. J. Nano-and bulk-silicon-based insertion anodes for lithium-ion secondary cells. *J. Power Sources* **163**, 1003–1039 (2007).
100. Saint, J. *et al.* Towards a fundamental understanding of the improved electrochemical performance of silicon–carbon composites. *Adv. Funct. Mater.* **17**, 1765–1774 (2007).
101. Choi, N.-S., Yao, Y., Cui, Y. & Cho, J. One dimensional Si/Sn-based nanowires and nanotubes for lithium-ion energy storage materials. *J. Mater. Chem.* **21**, 9825–9840 (2011).
102. Cho, J. Porous Si anode materials for lithium rechargeable batteries. *J. Mater. Chem.* **20**, 4009–4014 (2010).
103. Kim, H., Han, B., Choo, J. & Cho, J. Three-dimensional porous silicon particles for use in high-performance lithium secondary batteries. *Angew. Chem. Int. Ed.* **47**, 10151–10154 (2008).
104. Cheng, H. *et al.* Periodic porous silicon thin films with interconnected channels as durable anode materials for lithium ion batteries. *Mater. Chem. Phys.* **144**, 25–30 (2014).
105. Ge, M., Rong, J., Fang, X. & Zhou, C. Porous doped silicon nanowires for lithium ion battery anode with long cycle life. *Nano Lett.* **12**, 2318–2323 (2012).
106. Ge, M. *et al.* Large-scale fabrication, 3D tomography, and lithium-ion battery application of porous silicon. *Nano Lett.* **14**, 261–268 (2014).
107. Jia, Z. & Li, T. Stress-modulated driving force for lithiation reaction in hollow nano-anodes. *J. Power Sources* **275**, 866–876 (2015).
108. Li, J. C., Xiao, X. C., Cheng, Y. T. & Verbrugge, M. W. Atomic layered coating enabling ultrafast surface kinetics at silicon electrodes in lithium ion batteries. *J. Phys. Chem. Lett.* **4**, 3387–3391 (2013).
109. Ye, J. C. *et al.* Enhanced lithiation and fracture behavior of silicon mesoscale pillars via atomic layer coatings and geometry design. *J. Power Sources* **248**, 447–456 (2014).
110. Bogart, T. D. *et al.* Lithium ion battery peformance of silicon nanowires with carbon skin. *ACS Nano* **8**, 915–922 (2014).
111. Chatterjee, S. *et al.* Electrochemical and corrosion stability of nanostructured silicon by graphene coatings: toward high power porous silicon supercapacitors. *J. Phys. Chem. C* **118**, 10893–10902 (2014).
112. Chen, Y. L. *et al.* Pyrolytic carbon-coated silicon/carbon nanofiber composite anodes for high-performance lithium-ion batteries. *J. Power Sources* **298**, 130–137 (2015).
113. Fu, K. *et al.* Effect of CVD carbon coatings on Si@CNF composite as anode for lithium-ion batteries. *Nano Energy* **2**, 976–986 (2013).
114. Kim, H. & Cho, J. Superior lithium electroactive mesoporous si@carbon core –shell nanowires for lithium battery anode material. *Nano Lett.* **8**, 3688–3691 (2008).
115. Kong, J. H. *et al.* Silicon nanoparticles encapsulated in hollow graphitized carbon nanofibers for lithium ion battery anodes. *Nanoscale* **5**, 2967–2973 (2013).
116. Li, Q. Q. *et al.* Thickness-dependent fracture of amorphous carbon coating on SnO2 nanowire electrodes. *Carbon* **80**, 793–798 (2014).
117. Li, W. H. *et al.* Carbon-coated germanium nanowires on carbon nanofibers as self-supported electrodes for flexible lithium-ion batteries. *Small* **11**, 2762–2767 (2015).
118. Li, Z. F. *et al.* Novel pyrolyzed polyaniline-grafted silicon nanoparticles encapsulated in graphene sheets as li-ion battery anodes. *ACS Appl. Mater. Inter.* **6**, 5996–6002 (2014).
119. Zhang, F. *et al.* Pyrolytic carbon-coated Si nanoparticles on elastic graphene framework as anode materials for high-performance lithium-ion batteries. *Carbon* **82**, 161–167 (2015).
120. Zhao, G. Y., Zhang, L., Meng, Y. F., Zhang, N. Q. & Sun, K. N. High storage performance of core-shell Si@C nanoparticles as lithium ion battery anode material. *Mater. Lett.* **96**, 170–173 (2013).
121. Li, Y. *et al.* Tuning electrochemical performance of Si-based anodes for lithium-ion batteries by employing atomic layer deposition alumina coating. *J. Mater. Chem. A* **2**, 11417–11425 (2014).
122. Sandu, G. *et al.* Surface coating mediated swelling and fracture of silicon nanowires during lithiation. *ACS Nano* **8**, 9427–9436 (2014).
123. Kohandehghan, A. *et al.* Nanometer-scale Sn coatings improve the performance of silicon nanowire LIB anodes. *J. Mater. Chem. A* **2**, 11261–11279 (2014).
124. He, Y. *et al.* In situ transmission electron microscopy probing of native oxide and artificial layers on silicon nanoparticles for lithium ion batteries. *ACS Nano* **8**, 11816–11823 (2014).
125. Wu, H. *et al.* Stable Li-ion battery anodes by in-situ polymerization of conducting hydrogel to conformally coat silicon nanoparticles. *Nat. Commun.* **4**, 1943 (2013).
126. Wang, C. *et al.* Self-healing chemistry enables the stable operation of silicon microparticle anodes for high-energy lithium-ion batteries. *Nat. Chem* **5**, 1042–1048 (2013).
127. Luo, L. L. *et al.* Surface-coating constraint induced self-discharging of silicon nanoparticles as anodes for lithium ion batteries. *Nano Lett.* **15**, 7016–7022 (2015).
128. Wang, J. W., Liu, X. H., Mao, S. X. & Huang, J. Y. Microstructural evolution of tin nanoparticles during in situ sodium insertion and extraction. *Nano Lett.* **12**, 5897–5902 (2012).
129. Karki, K. *et al.* Lithium-assisted electrochemical welding in silicon nanowire battery electrodes. *Nano Lett.* **12**, 1392–1397 (2012).
130. Liu, X. H. *et al.* Reversible nanopore formation in ge nanowires during lithiation–delithiation cycling: an in situ transmission electron microscopy study. *Nano Lett.* **11**, 3991–3997 (2011).
131. Chen, Q. & Sieradzki, K. Spontaneous evolution of bicontinuous nanostructures in dealloyed Li-based systems. *Nat. Mater.* **12**, 1102–1106 (2013).
132. Choi, J. W. *et al.* Stepwise nanopore evolution in one-dimensional nanostructures. *Nano Lett.* **10**, 1409–1413 (2010).
133. Liang, W. *et al.* Nanovoid formation and annihilation in gallium nanodroplets under lithiation–delithiation cycling. *Nano Lett.* **13**, 5212–5217 (2013).
134. Chen, L. *et al.* Modulation of dendritic patterns during electrodeposition: a nonlinear phase-field model. *J. Power Sources* **300**, 376–385 (2015).
135. Liang, L. Y. & Chen, L. Q. Nonlinear phase field model for electrodeposition in electrochemical systems. *Appl. Phys. Lett.* **105**, 263903 (2014).
136. Liu, Z. *et al.* Interfacial study on solid electrolyte interphase at Li metal anode: implication for Li dendrite growth. *J. Electrochem. Soc.* **163**, A592–A598 (2016).